

Dephasing and error dynamics affecting a singlet-triplet qubit during coherent spin shuttling

Natalie D. Foster,^{1,*} Jacob D. Henshaw,¹ Martin Rudolph,¹ Dwight R. Luhman,¹ and Ryan M. Jock¹

¹*Sandia National Laboratories, Albuquerque, NM 87185, USA*

Quantum information transport over micron to millimeter scale distances is critical for the operation of practical quantum processors based on spin qubits. One method of achieving a long-range interaction is by coherent electron spin shuttling through an array of silicon quantum dots. In order to execute many shuttling operations with high fidelity, it is essential to understand the dynamics of qubit dephasing and relaxation during the shuttling process in order to mitigate them. However, errors arising after many repeated shuttles are not yet well documented. Here, we probe decay dynamics contributing to dephasing and relaxation of a singlet-triplet qubit during coherent spin shuttling over many N repeated shuttle operations. We find that losses are dominated by magnetic dephasing for small $N < 10^3$ and by incoherent shuttle errors for large $N > 10^3$. Additionally, we estimate shuttle error rates below 1×10^{-4} out to at least $N = 10^3$, representing an encouraging figure for future implementations of spin shuttling to entangle distant qubits.

INTRODUCTION

Spin qubits are a compelling candidate for the foundation of a quantum register network, having demonstrated single and two-qubit gate fidelities well over 99% [1, 2]. By reducing the spinful ^{29}Si nuclear background in silicon, isotopic enrichment enables coherent spin qubits to be hosted in foundry-compatible [3, 4] gate-defined quantum dots (QDs) [5, 6], streamlining integration with existing and rapidly advancing industrial silicon technology. Since spin qubit operations are carried out using short-range interactions often involving nearest neighbors [7–10], a scalable quantum computing architecture relying on long-range quantum information transfer using spin qubits could present a challenge. One solution is to build a remote qubit registry that facilitates information exchange over broad physical scales, leaving qubit operations to be carried out at dedicated local nodes [11, 12].

Linking quantum information between qubit nodes can be achieved in multiple ways. One example is by interfacing distant stationary qubit sites through an intermediate messenger, such as through virtual microwave photons to mediate remote spin-spin interactions in quantum transducers [13–15]. Another approach is to physically move the spin qubit; for example, by using surface acoustic waves to form a moving QD [16, 17], or by shuttling the spin controllably through an array of gate-defined electrostatic potential traps [18–21]. In the latter, the ability to perform many repeated shuttling operations with a low error rate is key to maintaining long-range qubit entanglement. A firm understanding of dephasing and relaxation sources during shuttling is therefore required. At present, these dynamics are not well quantified, especially out to the large number of shuttles needed to perform long-range interactions. For a spin qubit device composed of millions of qubits, for example, arranged on a crossbar array [22], thousands to tens of thousands of shuttling operations will need to be performed to link

sites on either end of the processor.

In this work, we categorize the main error sources and dynamics during electron spin shuttling by observing a singlet-triplet qubit over many repeated coherent shuttles of a single electron spin in a gate-defined Si/SiGe triple QD device. We focus first on expected shuttling-independent loss mechanisms – inhomogeneous dephasing and spin relaxation – and use this baseline to classify the nature of errors dependent on the number of shuttles (N). From Ramsey decay measurements carried out on the stationary qubit and the qubit during shuttling, we attribute the dominant error source occurring during shuttling for $N < 10^3$ to inhomogeneous dephasing arising from residual nuclear spins. We corroborate this finding by using dynamical decoupling to reduce magnetic noise and show it is independent of N , while also discovering the presence of nontrivial noise dynamics. From relaxation measurements, we define a bounding timescale expected of incoherent error processes in the qubit. We find, after implementing many repeated shuttling operations, that shuttling errors are incoherent but don't contribute appreciably to losses until $N > 10^3$, meaning that errors due to shuttling are small. Understanding the various noise mechanisms encountered during shuttling can aid the development of targeted mitigation strategies that will enable the completion of a large number of shuttles, allowing an opportunity for linking localized [23–25], and even deterministic [26], qubit nodes on a sparse qubit array.

Device overview and operation

Fig. 1a shows a schematic of the gate-defined triple QD device used in this work. Details of the device structure can be found in the Methods section. The electrochemical potential and electron occupation $n_{\text{QD}i}$ at each QD i are primarily controlled by voltages on plunger gates P_i , where $i = 0, 1, 2$ is the QD index. We de-

note the total charge occupation across the triple QD array by $(n_{\text{QD0}}, n_{\text{QD1}}, n_{\text{QD2}})$. The tunneling rate from the electron reservoir is controlled by a voltage applied to the barrier gate B0 and the tunnel coupling between adjacent QDs is controlled by barrier gates B1 and B2 (Fig. 1b).

We operate the device with four electrons in the QD chain, where two low-energy electrons under P0 form a filled-shell singlet and do not contribute significantly to the spin dynamics of the system [27, 28]. Fig. 1c shows an energy diagram of the remaining two-spin system illustrating the relationship between the singlet ($|S\rangle$) and triplet ($|T_0\rangle$, $|T_+\rangle$, $|T_-\rangle$) states in a small magnetic field. We employ a singlet-triplet (S - T_0) qubit [29], where the qubit is encoded in the $m = 0$ subspace of the 4-level system defined by linear combinations of the $|\uparrow\downarrow\rangle$ and $|\downarrow\uparrow\rangle$ states. Its logical states are defined as the eigenstates of the system in the limit of large exchange:

$$\begin{aligned} |0\rangle &= |S\rangle = \frac{1}{\sqrt{2}}(|\uparrow\downarrow\rangle - |\downarrow\uparrow\rangle) \\ |1\rangle &= |T_0\rangle = \frac{1}{\sqrt{2}}(|\uparrow\downarrow\rangle + |\downarrow\uparrow\rangle) \end{aligned} \quad (1)$$

A schematic of the pulse sequence used to initialize and measure the qubit is depicted in Fig. 1e, where we use an enhanced latching mechanism [30] of spin-to-charge conversion through Pauli spin blockade (PSB) to measure the qubit spin state [31–34]. Two-axis control of the qubit is achieved through baseband voltage pulses to modify barrier and QD chemical potentials and toggle between control regimes dominated by the exchange interaction, J , and the difference in electron Zeeman energy splitting between electrons in two QDs, ΔE_Z (Fig. 1d). We use voltage pulses applied to the B1 barrier gate and adjacent P0 and P1 QD gates at the exchange symmetric operating point [35, 36] to achieve rotations between $|\uparrow\downarrow\rangle$ and $|\downarrow\uparrow\rangle$. When the electrons are well isolated and exchange is turned off, $|S\rangle$ to $|T_0\rangle$ rotations are driven by [37]

$$\Delta E_Z = \Delta g \mu_B B, \quad (2)$$

where g is the g -factor, μ_B is the Bohr magneton, and B is the magnetic field. Differences in local magnetic fields or local g -factors both contribute to ΔE_Z . The unique B at each QD arises from external magnetic field gradients, or from the presence of residual spinful nuclei forming a random but slowly-varying Overhauser field [38, 39]. The difference in g -factor at each QD comes from variations in interface disorder across the Si/SiGe interface giving rise to local spin-orbit interactions [40, 41].

RESULTS

Coherent spin transfer

Two established approaches for spin shuttling [21] are conveyor mode [42–45] and bucket brigade mode [7, 18–20, 46]. Shuttling in this work is accomplished by a barrier pulse-assisted bucket brigade mode, in which we leverage individual gate voltage control to tailor the electrostatic potential landscape and move the spin between QDs. We prepare a $|S\rangle$ state and transfer one electron of the entangled spin pair from QD1 to QD2 (charge states (3,1,0) and (3,0,1), respectively) by detuning the voltages V_{P1} and V_{P2} (ramping in opposite directions), while simultaneously pulsing V_{B2} to lower the potential barrier and facilitate adiabatic transfer (Fig. 2a) (see discussion on Supplementary Fig. 1 for more details). We hold V_{B1} fixed to maintain negligible residual J with the electron in QD0 and ensure rotations about the Bloch sphere are facilitated by the dominant ΔE_Z interaction.

We first demonstrate spin transfer from one QD to another by examining qubit rotations in the region near the (3,1,0)-(3,0,1) charge transition. We apply an external magnetic field of $B_0 = 50$ mT in the plane of the Si quantum well to intentionally drive strong S - T_0 rotations in both charge regions, showing the spin is coherently transferred. Fig. 2b shows singlet return probability following a 6 μ s wait time at different QD1-QD2 detunings. This plot has four regions of interest describing different charge configurations. The bands in (3,1,0) and (3,0,1) describe differences in acquired singlet phase within each charge configuration due to changes in g modifying ΔE_Z as QD1 and QD2 are shaped by applied voltages, and the local interface disorder sampled by the electron varies [47]. The charge transition between the (3,1,0) and (3,0,1) appears as a diagonal strip of constant $\sim 50\%$ singlet return probability with no acquired phase accumulation visible, indicating a fully dephased qubit. A shift in coherent singlet return on either side of the transition indicates the spin is transferred from one isolated QD to the other (see discussion on Supplementary Fig. 2 for more details). The low singlet return probability and absence of acquired phase bands in (3,1,1) ((3,0,0)) is due to the addition (subtraction) of an electron to the system which rapidly destroys qubit coherence. Altogether, these four delineated regions map out the charge space where spin shuttling operations will be performed and show that the entangled electron spin may be coherently transferred between QD1 and QD2.

Spin coherence and sources of dephasing

To demonstrate spin coherence is preserved at each shuttle step and to quantify noise dynamics that drive dephasing independent of shuttling, we perform a Ram-

sey decay experiment by preparing a $|S\rangle$ state and letting it evolve under ΔE_Z . We measure the singlet return probability over time, averaged over 1 hour total to ensure the ergodic limit was reached [48] (Supplementary Fig. 3). Fig. 2c shows the singlet return at different locations on the charge stability map in Fig. 2b indicated as colored circles corresponding to (3,1,0), (3,0,1), and the charge transition.

We first consider dephasing in the case of negligible external magnetic field ($B_0 \approx 0$ mT) such that dephasing is expected to be dominated by fluctuations in the local Overhauser field [29], where no S - T_0 rotations are observed. We fit the data to a decay profile of the form

$$f_{T_2^*}(t) = Ae^{-(t/T_2^*)^\alpha} + y_0, \quad (3)$$

where A is the amplitude, y_0 is the vertical offset, T_2^* is the inhomogeneous dephasing time, and α is the decay exponent. The resulting dephasing times and fit uncertainties are $T_2^*(3,1,0) = 4.60 \pm 0.02 \mu\text{s}$, $T_2^*(3,0,1) = 3.86 \pm 0.02 \mu\text{s}$, and $T_2^*(\text{transition}) = 5.12 \pm 0.03 \mu\text{s}$, and are consistent with previously measured quantities for QDs in 800 ppm ^{29}Si [4, 49, 50]. The variation among T_2^* s suggest local sources of dephasing affect the spin in each QD, including the wavefunctions of nearby ^{29}Si and ^{73}Ge . We interpret the longer $T_2^*(\text{transition})$ as the result of a process like motional narrowing – effectively averaging out magnetic noise acquired from the different nuclear distributions when the spin is hybridized between QD1 and QD2 [21]. The resulting decay exponent fits, $\alpha(3,1,0) = 1.92 \pm 0.02$, $\alpha(3,0,1) = 2.16 \pm 0.02$, and $\alpha(\text{transition}) = 2.12 \pm 0.02$, resemble Gaussian profiles as expected of inhomogeneous nuclear spin dephasing [29].

Next, we apply a small external field of $B_0 = 50$ mT to amplify and study the effect of spin-orbit-driven charge noise acting on ΔE_Z . Clear S - T_0 oscillations are observed and fit to a decaying sine function of the form

$$f_{T_2^*}(t) = Ae^{-(t/T_2^*)^\alpha} \sin(2\pi ft) + y_0, \quad (4)$$

where f is the S - T_0 rotation frequency. The resulting dephasing times are $T_2^*(3,1,0) = 3.82 \pm 0.12 \mu\text{s}$, $T_2^*(3,0,1) = 4.09 \pm 0.03 \mu\text{s}$, and $T_2^*(\text{transition}) = 1.08 \pm 0.01 \mu\text{s}$. We attribute the fast decay observed at the charge transition to the hybridization of the electron wavefunction split between QD1 and QD2 [51], which is sensitive to charge noise. Charge noise arises from rapid fluctuations in spin-orbit interactions at the Si/SiGe interface that are intensified in an applied external magnetic field.

Additionally, we observe changes to α that imply changes to the noise spectrum. The resulting decay exponent fits are $\alpha(3,1,0) = 0.90 \pm 0.06$, $\alpha(3,0,1) = 2.12 \pm 0.06$, and $\alpha(\text{transition}) = 1.14 \pm 0.02$, ranging from exponential to Gaussian forms. Since it is the noise spectrum and mechanisms that dictate the observed decay profile [52], the spread in α suggests that different

localized noise dynamics, in addition to residual nuclear spins, contribute to dephasing in each QD. One possible source known to exhibit non-Gaussian decay behavior is random telegraph noise originating from charge traps [53], where the observed charge noise is often attributed to two-level systems (TLSs) that are distributed nonuniformly across the Si/SiGe interface [54]. This is consistent with our assessment that charge noise dominates the fast $T_2^*(\text{transition})$, and suggests an increased susceptibility to charge noise in QD1 compared to QD2, since $\alpha(3,1,0)$ is exponential and $\alpha(3,0,1)$ is Gaussian. Overall, we observe qubit dephasing to be primarily driven by fluctuations in the Overhauser fields generated by residual nuclear spins at 0 mT, and a combination of nuclear spins and charge noise at 50 mT.

Repeated spin shuttles

To understand the role of shuttle-induced errors, independent of intrinsic noise, we perform repeated spin shuttling operations to investigate errors from shuttling and observe the singlet return probability. We implement repetitions of the procedure outlined in the previous section to transfer an electron back and forth between QD1 and QD2. The voltage pulses are structured such that the shuttled electron spends an equal amount of time in each QD during shuttling ($2t_{\text{wait}}$), and the ramp time (t_{ramp}) is fixed at 10 ns between charge configurations to ensure adiabatic charge transfer. A single shuttle is defined as one transfer of an electron between QD1 and QD2 (from either of (3,1,0) or (3,0,1) to the other), where the total time spent shuttling N times is $t_{\text{shuttle}} = N(2t_{\text{wait}} + t_{\text{ramp}})$ (Fig. 3a).

To investigate dephasing during shuttling, we vary t_{wait} for a series of fixed N carried out within t_{shuttle} (Fig. 3c), with $B_0 \approx 0$ mT to minimize the charge noise-induced field-dependent noise dynamics on ΔE_Z discussed above. We observe a single decay profile in singlet return, independent of N , indicating the decay is primarily time-dependent. A decay fit of the form in Eq. 3 to the combined data reveals $T_2^* = 5.07 \pm 0.07 \mu\text{s}$, which is similar to $T_2^*(\text{transition})$ measured in the absence of shuttling and B_0 (Fig. 2c), and indicates the spin samples similar noise environments when shuttled and hybridized. This observation suggests the error introduced by the act of shuttling is low. The decay profile fits to a near-Gaussian with $\alpha = 1.82 \pm 0.07$, which points to the dominant dephasing mechanism being nuclear spin fluctuations.

Next, we employ a standard spin echo technique [50] to reduce the effect of slow magnetic noise and extend the qubit dephasing time. This allows more shuttle operations to be performed within the qubit coherence time, to further highlight the role of shuttle-induced error dynamics. For this experiment, $B_0 \approx 0$ mT to minimize field-

dependent effects on ΔE_Z . We prepare the $|S\rangle$ state and allow the two electron spins to evolve while one is stationary in QD0 and the other is repeatedly shuttled between QD1 and QD2 $N/2$ times. A calibrated J pulse on B1 applies a π_z operation to swap the two spins (Fig. 3b), followed by $N/2$ shuttles such that both spins sample the same magnetic environment for an equal amount of time, negating any acquired phase difference due to nuclear spin fluctuations slower than $1/2t_{\text{shuttle}}$. Fig. 3d shows the singlet return probability after implementing the spin echo sequence during shuttling for a range of N completed within t_{shuttle} . We observe a single decay profile independent of N and fit the data to a generic decay function of the form

$$f_{T_2^{\text{Hahn}}}(t) = Ae^{-(t/T_2^{\text{Hahn}})^\alpha} + y_0, \quad (5)$$

similar to Eq. 3. The fit yields $T_2^{\text{Hahn}} = 84.48 \pm 7.82 \mu\text{s}$ which is reasonably consistent with previously measured values in Si/SiGe heterostructures [55, 56], and indicates sources of noise contributing to dephasing have been reduced. The fit converges with an exponent of $\alpha = 0.64 \pm 0.06$, which deviates from α commonly observed in the range of $1 \lesssim \alpha \lesssim 2$ [29, 55, 57, 58], suggesting a different noise spectrum is introduced. In other systems, sub-exponential decoherence behavior has been theorized to originate from 2D electron surfaces [59], and has recently been predicted in 2D electron spin baths in NV⁻ centers in diamond [60]. The sub-exponential decay behavior observed here points to nontrivial noise dynamics of this nature affecting the qubit.

Next, we investigate the role of spin relaxation during shuttling since spin-flip mechanisms are known error sources in Si QDs [61]. We prepare an eigenstate $|\uparrow\downarrow\rangle_{(3,1,0)}$ of the ΔE_Z interaction and monitor return of this state while repeatedly shuttling between QD1 and QD2. We used a small applied field of $B_0 = 10 \text{ mT}$ to avoid mixing with $|T_-\rangle$ during the (3,1,0) charge state preparation. Fig. 3e shows singlet return probability of the shuttled $|\uparrow\downarrow\rangle$ state for a range of N completed within t_{shuttle} . We observe a single decay profile independent of N and fit the data to an exponential decay function of the form

$$f_{T_1}(t) = Ae^{-t/T_1} + y_0 \quad (6)$$

with a range of assumptions placed on y_0 , the singlet return saturation, since it is not explicitly measured. The fit results in $T_1 = 6.22 \pm 0.71 \text{ ms}$, where the uncertainty represents fit variation based on y_0 , and lies within the broad range of T_1 measured for electrons confined to Si QDs, typically falling between milliseconds and seconds [49, 61–63]. A variety of mechanisms generally stemming from spin-orbit and spin-valley interactions contribute to spin relaxation in Si QDs [64, 65]. Due to the natural disorder and inversion asymmetry at the Si/SiGe interface, the small in-plane B_0 , as well as shuttling itself, give rise

to spin-orbit effects [50] that can induce spin flip relaxation over time. At $B_0 = 10 \text{ mT}$, we expect a small but non-negligible influence from the spin-valley hotspot measured near 190 mT in QD0 (see discussion on Supplementary Fig. 4), which could drive a faster relaxation rate (T_1^{-1}) [61]. Very few references for T_1 in the low-field limit exist; however, the observation that $T_1 > T_2^{\text{Hahn}}$ in our device shows that incoherent errors due to spin-flip processes during shuttling are relatively small compared to coherent errors arising from magnetic noise.

From the data presented in Figs. 3c, d, and e, we anticipate the shuttling error to be low since the time-dependent singlet return decays in each panel are nearly indistinguishable among different N . To assess the time-independent error due to the shuttling operation, we fix t_{shuttle} while varying N such that the effect of time-dependent dephasing and errors is constant with N . Figs. 3f, g, and h show the measured singlet return probability at three fixed t_{shuttle} corresponding to the shuttling experiments shown in the insets of Figs. 3c, d, and e, respectively. The error bars represent standard deviations of the mean of singlet return spanning repeated measurements totaling at least one hour. In all cases, the decay in singlet return is undetectable within error bars, and suggests shuttle errors are negligible out to at least $N = 10^3$ (Fig. 3g). We make an attempt to quantify the worst-case estimate of shuttling error by fitting a simple linear function from the top of the first error bar to the bottom of the last error bar and extracting the slope of the line (not shown), which bounds the error per shuttle below 1×10^{-4} , an improvement from recently reported shuttling errors [20, 45].

Due to the low shuttling error, many repeated N are required to identify and elucidate the nature of shuttle-induced losses. To do so we extend the previously discussed spin echo shuttling experiment out to the maximum N possible within our instrument bandwidth capabilities. We compose a shuttling experiment at $B_0 \approx 0 \text{ mT}$ to reduce field-dependent noise, with the minimum possible $2t_{\text{wait}} = 4 \text{ ns}$ and increase the repeated shuttles out to $N = 4 \times 10^5$, spanning a total time of $t_{\text{shuttle}} = 5.6 \text{ ms}$, where $t_{\text{shuttle}}(N) = 14N \text{ ns}$. The singlet return probability over N , and equivalent t_{shuttle} , is shown in Fig. 4. We consider the observed decay in the context of estimated T_2^{Hahn} and T_1 dynamics in this device, which are presented as shaded colored regions and are scaled by a multiplicative factor accounting for SPAM variation, serving as a guide to the eye. For a small number of shuttles $N < 10^3$, the T_2^{Hahn} decay profile agrees with the data and implies the decay is dominated by the non-trivial spectral noise acting on ΔE_Z . For a large number of shuttles $N > 10^3$, the decay deviates from this behavior and appears to be dominated by a different mechanism. The observation that the singlet return saturates below 50% indicates that the shuttling error is due to an incoherent spin relaxation process. The process causes

decay on a timescale faster than the measured T_1 (for $N < 10^3$), indicating a shuttle-induced, or N -dependent mechanism dominating spin relaxation when shuttling a large number of times ($N > 10^3$).

To characterize the nature of the shuttling error as a function of the number of shuttles, we fit to the data a phenomenological function of the form

$$f_{N^*}(N) = Ae^{-(N/N^*)^\alpha} + y_0, \quad (7)$$

which defines the characteristic decay in units of N (N^*). The fit results in a sub-exponential $\alpha = 0.41 \pm 0.03$, which suggests the presence of noise mechanisms that deviate from both a typical $1/f$ -like noise spectrum observed for simple dephasing [29, 66] and a simple exponential decay expected of relaxation [63, 67]. The observation that the function fits poorly for smaller $N < 10^3$ suggests the influence of shuttle errors do not become apparent until after the completion of $N \sim 10^3$ shuttles. From the fit we also find $N^* = (1.92 \pm 0.32) \times 10^4$ shuttles can be completed within a shuttle error-limited characteristic decay period, an order of magnitude more than recently demonstrated with shuttled spins [20, 46]. Although a single decay profile is insufficient to describe the losses observed during shuttling, it points to the complexity of competing noise and error mechanisms at play during shuttling as N increases.

DISCUSSION

Understanding sources of error during shuttling is essential to the development of a successful spin shuttling platform used to entangle remote qubits. In this work, we have built on previous efforts exploring bucket brigade mode shuttling in Si [7, 51] and in Ge [20]. Using an enhanced barrier pulse-assisted approach, we have demonstrated coherent spin shuttling in the limit of a large number of shuttles, with the goal of categorizing the different dephasing and relaxation mechanisms affecting the qubit while shuttling. Independent of shuttling, we identify magnetic noise from Overhauser field fluctuations as the dominant source of dephasing in the absence of external fields ($B_0 \approx 0$ mT) and a combination of nuclear bath noise and charge noise originating from TLSs at the Si/SiGe interface at finite field ($B_0 = 50$ mT). When the spin is repeatedly shuttled, we observe little change in this decay at $B_0 \approx 0$ mT, indicating that shuttling operations negligibly contribute to losses. Using a standard spin echo technique, we show coherence time during shuttling may be extended owing to the reduction of magnetic noise on ΔE_Z and is limited by a different noise spectrum indicated by a subexponential T_2^{Hahn} decay profile. Residual unfiltered magnetic noise on T_2^{Hahn} timescales is determined to be the limiting time-dependent contribution since $T_2^{\text{Hahn}} < T_1$. Additionally, we find that T_2^* ,

T_2^{Hahn} , and T_1 are N -independent in the regime examined in this work and do not contribute appreciably to shuttling error.

By executing shuttle operations out to $N = 4 \times 10^5$, we are able to identify a shuttling-induced incoherent error which contributes significantly only after many shuttle operations. In the small $N (< 10^3)$ regime, shuttling errors are negligible and decay is primarily limited by residual magnetic dephasing on T_2^{Hahn} timescales. In the large $N (> 10^3)$ regime, a shuttle-induced, or N -dependent mechanism driving spin relaxation causes decay on a timescale faster than the measured T_1 (for $N < 10^3$), which dominates and limits decay during the shuttling sequence. In the absence of temporal dephasing and relaxation (Figs. 3f., g., h.), we made a rudimentary yet encouraging shuttle error estimate of 1×10^{-4} . A more thorough assessment is required to elucidate the details of this N -dependent process. Future work is required to improve characterization of the noise spectrum affecting the qubit during shuttling in order to extend shuttling capability, which can be done, for example, by spectrally targeting coherent noise on the gates [66].

Lastly, we make estimates of the error per shuttle based on decay assumptions for 14 ns shuttling operations, summarized in Table I. Of the dynamics described by the three error regimes evaluated in this work, error estimates based on the T_2^* and T_1 decays represent the more practical expectation for building up a long-range spin shuttling platform. If fluctuating Overhauser fields are the only noise mechanism and decay is limited by T_2^* , we extrapolate the shuttling error to 2.2×10^{-5} . In the case that spin-flip relaxation on the T_1 timescale limits decay, the error is estimated at 2.3×10^{-6} . These results highlight the potential for low-error shuttling as a promising pathway to enabling distant spin entanglement in quantum computing platforms.

METHODS

Device details

The device was fabricated by Intel Corporation and is based on a Si/Si_{0.7}Ge_{0.3} heterostructure [4], where the quantum well is composed of isotopically-purified ^{28}Si (800 ppm ^{29}Si). Gate-defined QDs are formed by molding the local electrostatic potential with voltages applied to the surrounding gates. A reservoir of electrons is hosted under the accumulation gate AC0 from which the QDs are populated. Changes in charge occupation are sensed by a single electron transistor (SET) located at a dedicated QD on the top half of the device opposite the qubit QDs and isolated by a center screening gate. The dot pitch is ~ 120 nm and the well width is ~ 5 nm.

Shuttle experiment	Decay fit	Lifetime (τ)	Exponent (α)	Error per shuttle (p)
Ramsey	Gaussian	$T_2^* = 5.07 \pm 0.07 \mu\text{s}$	1.82 ± 0.07	2.2×10^{-5}
Relaxation	Exponential	$T_1 = 6.22 \pm 0.71 \text{ ms}$	1 (fixed)	2.3×10^{-6}

Table I. Shuttle errors based on decay fit calculated from the time it takes to complete one shuttle ($p = 1 - e^{-(14 \text{ ns}/\tau)^\alpha}$)

Experimental setup

We used a closed-loop dry cryostat Bluefors LD400 dilution refrigerator with a base temperature of 7 mK. The electron temperature was approximately 250 mK. We used a heterojunction bipolar transistor (HBT) operating at -1.056 V emitter bias on the readout SET line to perform cryogenic preamplification [68]. DC voltage to the gates was supplied by a QDevil QDAC II and fast AC pulses were generated by a Keysight M3201 AWG with a 500 MHz sampling rate. DC and fast voltage pulses are combined through a cryogenic RC bias tee at the PCB. Each individual spin state measurement is acquired over an average of 100 shots. We used one axis of a superconducting vector magnet aligned to the [110] crystal direction in the plane of the device, perpendicular to the direction of shuttling.

REFERENCES

-
- * Corresponding author: ndfoste@sandia.gov
- [1] Yoneda, J. *et al.* A quantum-dot spin qubit with coherence limited by charge noise and fidelity higher than 99.9%. *Nat Nanotechnol* **13**, 102–106 (2018).
 - [2] Mills, A. R. *et al.* Two-qubit silicon quantum processor with operation fidelity exceeding 99%. *Science Advances* **8**, eabn5130 (2022).
 - [3] Zwerger, A. M. J. *et al.* Qubits made by advanced semiconductor manufacturing. *Nature Electronics* **5**, 184–190 (2022).
 - [4] Neyens, S. *et al.* Probing single electrons across 300-mm spin qubit wafers. *Nature* **629**, 80–85 (2024).
 - [5] Wiel, W. G. v. d., Stopa, M., Koder, T., Hatano, T. & Tarucha, S. Semiconductor quantum dots for electron spin qubits. *New Journal of Physics* **8**, 28–28 (2006).
 - [6] Burkard, G., Ladd, T. D., Pan, A., Nichol, J. M. & Petta, J. R. Semiconductor spin qubits. *Reviews of Modern Physics* **95** (2023).
 - [7] Noiri, A. *et al.* A shuttling-based two-qubit logic gate for linking distant silicon quantum processors. *Nat Commun* **13**, 5740 (2022).
 - [8] Watson, T. F. *et al.* A programmable two-qubit quantum processor in silicon. *Nature* **555**, 633–637 (2018).
 - [9] Xue, X. *et al.* Quantum logic with spin qubits crossing the surface code threshold. *Nature* **601**, 343–347 (2022).
 - [10] Sigillito, A. J. *et al.* Site-selective quantum control in an isotopically enriched $\text{si}^{28}/\text{si}^{0.7}\text{ge}^{0.3}$ quadruple quantum dot. *Physical Review Applied* **11** (2019).
 - [11] Van Meter, R. & Horsman, D. A blueprint for building a quantum computer. *Communications of the ACM* **56**, 84–93 (2013).
 - [12] Vandersypen, L. M. K. *et al.* Interfacing spin qubits in quantum dots and donors—hot, dense, and coherent. *npj Quantum Information* **3** (2017).
 - [13] Mi, X. *et al.* A coherent spin-photon interface in silicon. *Nature* **555**, 599–603 (2018).
 - [14] Borjans, F., Croot, X. G., Mi, X., Gullans, M. J. & Petta, J. R. Resonant microwave-mediated interactions between distant electron spins. *Nature* **577**, 195–198 (2020).
 - [15] Harvey-Collard, P. *et al.* Coherent spin-spin coupling mediated by virtual microwave photons. *Physical Review X* **12** (2022).
 - [16] Takada, S. *et al.* Sound-driven single-electron transfer in a circuit of coupled quantum rails. *Nat Commun* **10**, 4557 (2019).
 - [17] Jadot, B. *et al.* Distant spin entanglement via fast and coherent electron shuttling. *Nat Nanotechnol* **16**, 570–575 (2021).
 - [18] Flentje, H. *et al.* Coherent long-distance displacement of individual electron spins. *Nat Commun* **8**, 501 (2017).
 - [19] Fujita, T., Baart, T. A., Reichl, C., Wegscheider, W. & Vandersypen, L. M. K. Coherent shuttle of electron-spin states. *npj Quantum Information* **3** (2017).
 - [20] van Riggelen-Doelman, F. *et al.* Coherent spin qubit shuttling through germanium quantum dots. *arXiv:2308.02406* (2023).
 - [21] Langrock, V. *et al.* Blueprint of a scalable spin qubit shuttle device for coherent mid-range qubit transfer in disordered $\text{si}/\text{si}_{0.9}\text{ge}_{0.1}$. *PRX Quantum* **4** (2023).
 - [22] Borsoi, F. *et al.* Shared control of a 16 semiconductor quantum dot crossbar array. *Nat Nanotechnol* **19**, 21–27 (2024).
 - [23] Morton, J. J. L. *et al.* Solid-state quantum memory using the ^{31}P nuclear spin. *Nature* **455**, 1085–1088 (2008).
 - [24] Pla, J. J. *et al.* High-fidelity readout and control of a nuclear spin qubit in silicon. *Nature* **496**, 334–8 (2013).
 - [25] Witzel, W. M., Lutz, J. J. & Luhman, D. R. Remarkable prospect for quantum-dot-coupled tin qubits in silicon. *PRX Quantum* **3** (2022).
 - [26] Jakob, A. M. *et al.* Deterministic shallow dopant implantation in silicon with detection confidence upper-bound to 99.85% by ion-solid interactions. *Adv Mater* **34**, e2103235 (2022).
 - [27] Higginbotham, A. P., Kuemmeth, F., Hanson, M. P., Gossard, A. C. & Marcus, C. M. Coherent operations and screening in multielectron spin qubits. *Phys Rev Lett* **112**, 026801 (2014).
 - [28] Harvey-Collard, P. *et al.* Coherent coupling between a quantum dot and a donor in silicon. *Nat Commun* **8**, 1029 (2017).
 - [29] Petta, J. R. *et al.* Coherent manipulation of coupled electron spins in semiconductor quantum dots. *Science* **309**, 2180–2184 (2005).

- [30] Harvey-Collard, P. *et al.* High-fidelity single-shot readout for a spin qubit via an enhanced latching mechanism. *Physical Review X* **8** (2018).
- [31] Johnson, A. C., Petta, J. R., Marcus, C. M., Hanson, M. P. & Gossard, A. C. Singlet-triplet spin blockade and charge sensing in a few-electron double quantum dot. *Physical Review B* **72** (2005).
- [32] Lai, N. S. *et al.* Pauli spin blockade in a highly tunable silicon double quantum dot. *Sci Rep* **1**, 110 (2011).
- [33] Zhao, R. *et al.* Single-spin qubits in isotopically enriched silicon at low magnetic field. *Nat Commun* **10**, 5500 (2019).
- [34] Jang, W. *et al.* Robust energy-selective tunneling readout of singlet-triplet qubits under large magnetic field gradient. *npj Quantum Information* **6** (2020).
- [35] Martins, F. *et al.* Noise suppression using symmetric exchange gates in spin qubits. *Phys Rev Lett* **116**, 116801 (2016).
- [36] Reed, M. D. *et al.* Reduced sensitivity to charge noise in semiconductor spin qubits via symmetric operation. *Phys Rev Lett* **116**, 110402 (2016).
- [37] Jock, R. M. *et al.* A silicon singlet-triplet qubit driven by spin-valley coupling. *Nat Commun* **13**, 641 (2022).
- [38] Koppens, F. H. L. *et al.* Control and detection of singlet-triplet mixing in a random nuclear field. *Science* **309**, 1346–1350 (2005).
- [39] Coish, W. A., Fischer, J. & Loss, D. Exponential decay in a spin bath. *Physical Review B* **77** (2008).
- [40] Prada, M., Klimeck, G. & Joynt, R. Spin-orbit splittings in si/sige quantum wells: from ideal si membranes to realistic heterostructures. *New Journal of Physics* **13** (2011).
- [41] Jiang, Z., Kharche, N., Boykin, T. & Klimeck, G. Effects of interface disorder on valley splitting in sige/si/sige quantum wells. *Applied Physics Letters* **100** (2012).
- [42] Mills, A. R. *et al.* Computer-automated tuning procedures for semiconductor quantum dot arrays. *Applied Physics Letters* **115** (2019).
- [43] Seidler, I. *et al.* Conveyor-mode single-electron shuttling in si/sige for a scalable quantum computing architecture. *npj Quantum Information* **8** (2022).
- [44] Xue, R. *et al.* Si/sige qubus for single electron information-processing devices with memory and micron-scale connectivity function. *arXiv:2306.16375* (2023).
- [45] Struck, T. *et al.* Spin-epr-pair separation by conveyor-mode single electron shuttling in si/sige. *Nat Commun* **15**, 1325 (2024).
- [46] Zwerver, A. M. J. *et al.* Shuttling an electron spin through a silicon quantum dot array. *PRX Quantum* **4** (2023).
- [47] Liu, Y. Y. *et al.* Magnetic-gradient-free two-axis control of a valley spin qubit in sixgel-x. *Physical Review Applied* **16** (2021).
- [48] Madzik, M. T. *et al.* Controllable freezing of the nuclear spin bath in a single-atom spin qubit. *Science Advances* **6**, eaba3442 (2020).
- [49] Eng, K. *et al.* Isotopically enhanced triple-quantum-dot qubit. *Science Advances* **1**, e1500214 (2015).
- [50] Jock, R. M. *et al.* A silicon metal-oxide-semiconductor electron spin-orbit qubit. *Nat Commun* **9**, 1768 (2018).
- [51] Yoneda, J. *et al.* Coherent spin qubit transport in silicon. *Nat Commun* **12**, 4114 (2021).
- [52] Stano, P. & Loss, D. Review of performance metrics of spin qubits in gated semiconducting nanostructures. *Nature Reviews Physics* **4**, 672–688 (2022).
- [53] Culcer, D., Hu, X. & Das Sarma, S. Dephasing of si spin qubits due to charge noise. *Applied Physics Letters* **95** (2009).
- [54] Connors, E. J., Nelson, J. J., Qiao, H., Edge, L. F. & Nichol, J. M. Low-frequency charge noise in si/sige quantum dots. *Physical Review B* **100** (2019).
- [55] Kawakami, E. *et al.* Electrical control of a long-lived spin qubit in a si/sige quantum dot. *Nat Nanotechnol* **9**, 666–70 (2014).
- [56] Kerckhoff, J. *et al.* Magnetic gradient fluctuations from quadrupolar ⁷³ge in si / sige exchange-only qubits. *PRX Quantum* **2** (2021).
- [57] Veldhorst, M. *et al.* An addressable quantum dot qubit with fault-tolerant control-fidelity. *Nat Nanotechnol* **9**, 981–5 (2014).
- [58] Kobayashi, T. *et al.* Engineering long spin coherence times of spin-orbit qubits in silicon. *Nature Materials* **20**, 38–42 (2021).
- [59] Witzel, W. M., Carroll, M. S., Cywinski, L. & Das Sarma, S. Quantum decoherence of the central spin in a sparse system of dipolar coupled spins. *Physical Review B* **86** (2012).
- [60] Schatzle, P. *et al.* Extended spin-coherence time in strongly-coupled spin baths in quasi two-dimensional layers. *arXiv:2401.16169* (2024).
- [61] Yang, C. H. *et al.* Spin-valley lifetimes in a silicon quantum dot with tunable valley splitting. *Nat Commun* **4**, 2069 (2013).
- [62] Simmons, C. B. *et al.* Tunable spin loading and t1 of a silicon spin qubit measured by single-shot readout. *Phys Rev Lett* **106**, 156804 (2011).
- [63] Petit, L. *et al.* Spin lifetime and charge noise in hot silicon quantum dot qubits. *Phys Rev Lett* **121**, 076801 (2018).
- [64] Tahan, C. & Joynt, R. Relaxation of excited spin, orbital, and valley qubit states in ideal silicon quantum dots. *Physical Review B* **89** (2014).
- [65] Borjans, F., Zajac, D. M., Hazard, T. M. & Petta, J. R. Single-spin relaxation in a synthetic spin-orbit field. *Physical Review Applied* **11** (2019).
- [66] Connors, E. J., Nelson, J., Edge, L. F. & Nichol, J. M. Charge-noise spectroscopy of si/sige quantum dots via dynamically-decoupled exchange oscillations. *Nat Commun* **13**, 940 (2022).
- [67] Simmons, S. *et al.* Entanglement in a solid-state spin ensemble. *Nature* **470**, 69–72 (2011).
- [68] Curry, M. J. *et al.* Single-shot readout performance of two heterojunction-bipolar-transistor amplification circuits at millikelvin temperatures. *Sci Rep* **9**, 16976 (2019).
- [69] Yang, C. H. *et al.* Orbital and valley state spectra of a few-electron silicon quantum dot. *Physical Review B* **86** (2012).

ACKNOWLEDGMENTS

We gratefully acknowledge Intel Corp. for providing devices and Matthew Curry, Lester Lampert and Nathan Bishop for helpful discussions on devices operation and performance. We thank Charlotte I. Evans for offering

advice on measurement acquisition software usage. We also thank Wayne M. Witzel and N. Toby Jacobson for fruitful conversations regarding the observed decay dynamics. Sandia National Laboratories is a multi-mission laboratory managed and operated by National Technology & Engineering Solutions of Sandia, LLC (NTESS), a wholly owned subsidiary of Honeywell International Inc., for the U.S. Department of Energy's National Nuclear Security Administration (DOE/NNSA) under contract DE-NA0003525. This written work is authored by an employee of NTESS. The employee, not NTESS, owns the right, title and interest in and to the written work and is responsible for its contents. Any subjective views or opinions that might be expressed in the written work do not necessarily represent the views of the U.S. Government. The publisher acknowledges that the U.S. Government retains a non-exclusive, paid-up, irrevocable, world-wide license to publish or reproduce the published form of this written work or allow others to do so, for U.S. Government purposes. The DOE will provide public access to results of federally sponsored research in accordance with the DOE Public Access Plan.

AUTHOR CONTRIBUTIONS

N.D.F. and R. M. J. designed the experiments. N. D. F. performed the experiments and analyzed the data. N. D. F., J. D. H., and R. M. J. discussed the results. J. D. H. and M. R. contributed to the measurement setup and performed initial shuttling demonstrations. N. D. F. wrote the manuscript with input from all co-authors. R. M. J. and D. R. L. supervised the project.

SUPPLEMENTARY INFORMATION

Barrier pulsing

For barrier-assisted bucket brigade shuttling we pulse the B2 barrier gate to increase the coupling between QD1 and QD2 and ensure adiabatic spin transfer. Supplementary Fig. 1 shows a series of singlet return probability raster scans in the P1-P2 voltage space (left column), accompanied by linear detuning ramps of V_{P1} and V_{P2} (ramped in opposite directions) from (3,1,0) to (3,0,1) over time (right column). Nominally $V_{B2}^0 = 0.81$ V before the transfer, and $\text{dB2} = V_{B2} - V_{B2}^0$ V. For high barrier (small dB2, first row), the electron spin is transferred to (3,0,1) with low fidelity evidenced by the decrease in oscillation amplitude. The appearance of multiple S - T_0 oscillation frequencies in the first three rows with $\text{dB2} = 0.100, 0.125, 0.150$ V (panels f.-h.) suggest the possibility of leakage into excited valley-orbit states [69] during transfer. For $\text{dB2} = 0.175, 0.200$ V in the last two rows, the $|S\rangle$ return probability is similar for both charge

configurations, indicating the electron spin is transferred with minimal coherence loss while preserving the individual character of the QDs. The quickly dephasing singlet at the charge transition in panels f.-j. suggests the electron is strongly hybridized in both QDs. The criteria used to select dB2 for the experiments were singlet visibility preservation during the transfer and clear distinction of the charge transition, which are optimal in the case of $\text{dB2} = 0.200$ V.

Characterizing Δg and the interdot charge transition

We expect the rotation frequency f to increase linearly with B_0 at a rate $\Delta g_{i,j} \mu_B / h$ defined for each pair of QD*i* and QD*j*, where h is the Planck constant from the expression $E = hf$. We measured the singlet return probability as a function of wait time in each charge configuration (3,1,0) and (3,0,1), while an in-plane B_0 oriented along the [110] crystallographic axis was ramped from 0 to 300 mT. Supplementary Fig. 4 shows the raw data and normalized fast Fourier transforms, demonstrating S - T_0 rotation frequency increasing linearly with B_0 at lower fields for both QD0-QD1 and QD0-QD2 pairs, as expected. Linear fits to the data result in distinct slopes of 42.47 ± 0.21 MHz/T for QD0-QD1, and 36.26 ± 0.71 MHz/T for QD0-QD2 from which we estimated Δg -factors of $|\Delta g_{0,1}| = 0.0030$ and $|\Delta g_{0,2}| = 0.0026$. The observation of rapid S - T_0 rotations and divergence in frequency for both charge configurations near $B_0 = 190$ mT suggests the presence of strong spin-valley coupling in QD0, the dot common to both configurations [37]. The appearance of a second divergence near $B_0 = 0.3$ T could be the emergence of a weakly coupled higher-energy valley state that is more pronounced in QD1 than in QD2. Nonetheless, for the low fields used in this work ($B_0 = 0$ to 50 mT), we expect the influence of these unexplored features to be minimal.

We analyze the nature of the interdot charge transition in closer detail in Supplementary Fig. 2 by transferring the prepared qubit state between QD1 and QD2 and observing the singlet return probability over time. Supplementary Fig. 2a. shows measured S - T_0 rotations in both charge sectors, and Fig. 2b. shows the results of dephasing sine (Eq. 4) fits to each time-trace in the data. We observe a clear distinction in T_2^* based on detuning (~ 6 μs in (3,1,0), ~ 4.5 μs in (3,0,1) and ~ 1 μs at the charge transition), as well as a gradual decrease in S - T_0 rotation frequency (from ~ 2.41 to ~ 2.12 MHz) as detuning is ramped from (3,1,0) to (3,0,1) that appears to flatten off farther from the charge transition. We note that the T_2^* values obtained using this fit are slightly longer than the values reported for the data in Fig. 2c, and conclude that this is expected of data averaged well below the ergodic limit [48] (see discussion on Supplementary Fig. 3 for more information). Over-

all, these observations demonstrate that the electron is well-isolated in QD1 or QD2 because the qubit is shown

to experience unique $|S\rangle$ - $|T_0\rangle$ rotation frequencies due to unique Δg pertaining to each QD.

fit parameter	(3,1,0) at 0 mT	(3,0,1) at 0 mT	transition at 0 mT	(3,1,0) at 50 mT	(3,0,1) at 50 mT	transition at 50 mT
A ($ S\rangle$ %)	0.325 ± 0.002	0.354 ± 0.002	0.318 ± 0.002	0.342 ± 0.009	0.330 ± 0.003	0.321 ± 0.003
T_2^* (μ s)	4.60 ± 0.03	3.86 ± 0.01	5.12 ± 0.03	3.82 ± 0.12	4.09 ± 0.03	1.08 ± 0.01
α (a. u.)	1.92 ± 0.03	2.16 ± 0.03	2.10 ± 0.03	0.90 ± 0.06	2.12 ± 0.06	1.14 ± 0.02
f (MHz)	-	-	-	2.4031 ± 0.0008	2.0356 ± 0.0007	2.3516 ± 0.0010
y_0 ($ S\rangle$ %)	0.374 ± 0.001	0.408 ± 0.001	0.399 ± 0.001	0.473 ± 0.001	0.481 ± 0.001	0.4640 ± 0.0001

Table II. Fit parameters and uncertainties for Ramsey experiment shown in Fig. 2c.

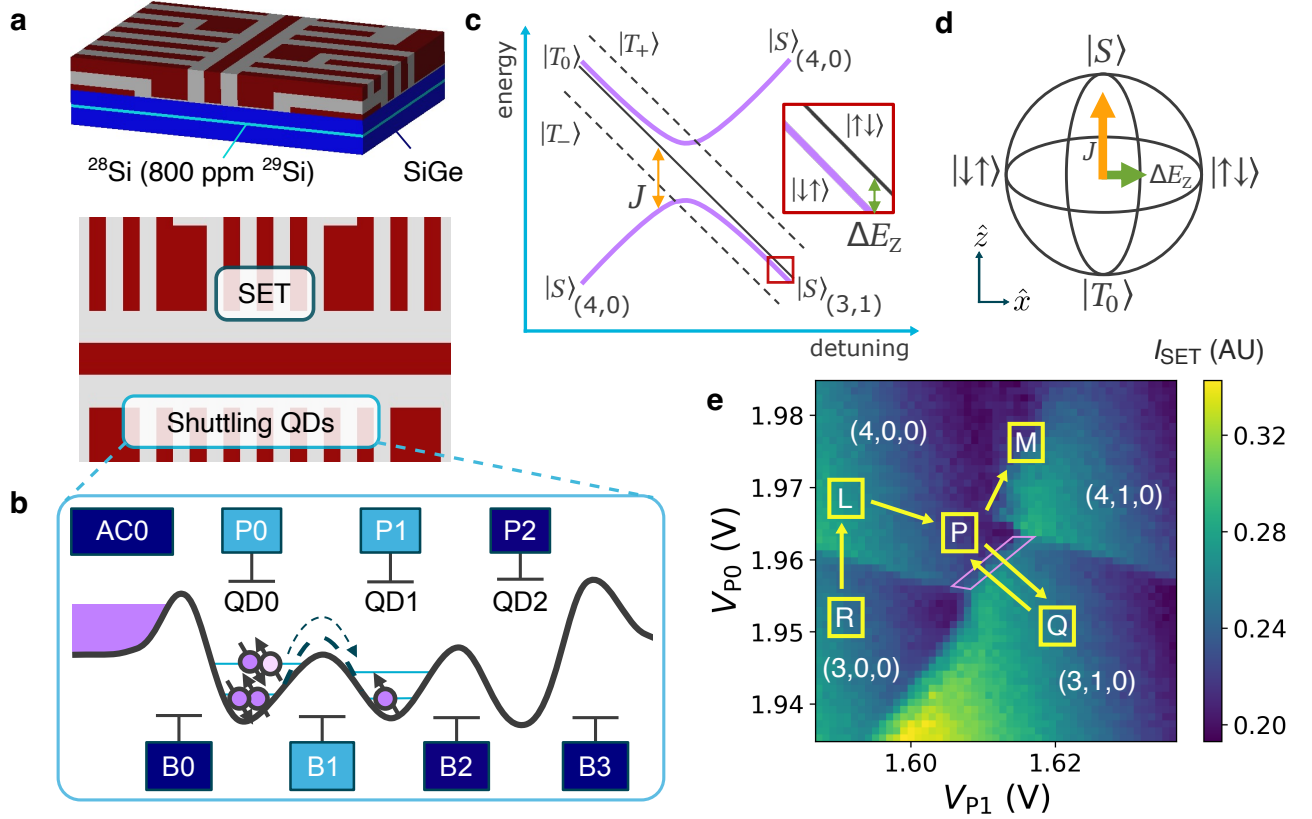


Figure 1. Singlet-triplet qubit in a triple quantum dot device. **a.** 3D profile of the device showing the ^{28}Si quantum well (light blue) buried within SiGe (dark blue), overlapping metal gates (maroon) and oxide (gray) (above). 2D overview of the device with relevant gates composing the SET and the shuttling QDs encircled (below). **b.** Cartoon schematic of the electrostatic potential in the shuttling QDs depicting the charge transition between (4,0,0) and (3,1,0). The electron reservoir is shown under accumulation gate AC0 in purple. Electron spins ordered on energy levels (light blue horizontal lines) are moved between adjacent QDs by applying voltages to the plunger (P) and barrier (B) gates in light blue. Voltages on other gates in dark blue are nominally static. **c.** Energy diagram of the $S-T_0$ qubit in an applied magnetic field. J is defined between $|S\rangle$ and $|T_0\rangle$ states. ΔE_Z separates the $|\uparrow\downarrow\rangle$ and $|\downarrow\uparrow\rangle$ states. $|\uparrow\downarrow\rangle$ is arbitrary in permutation and cannot be distinguished from $|\downarrow\uparrow\rangle$, but is used throughout for simplicity. **d.** $S-T_0$ Bloch sphere corresponding to the energy diagram in **c.** showing orthogonal energy components J and ΔE_Z . **e.** Charge stability map formed by varying P0 and P1 gate voltages showing charge transitions between QD0 and QD1. The qubit is reset in (3,0,0) for 140 μ s (R), then loaded into (4,0,0) (L), rolled near the (4,0,0)–(3,1,0) PSB region (approximate location outlined in pink) to prepare for transfer (P), and then transferred by rapid adiabatic passage to (3,1,0) (Q). The spin state is measured by latched PSB at the (4,0,0)–(4,1,0) boundary (M).

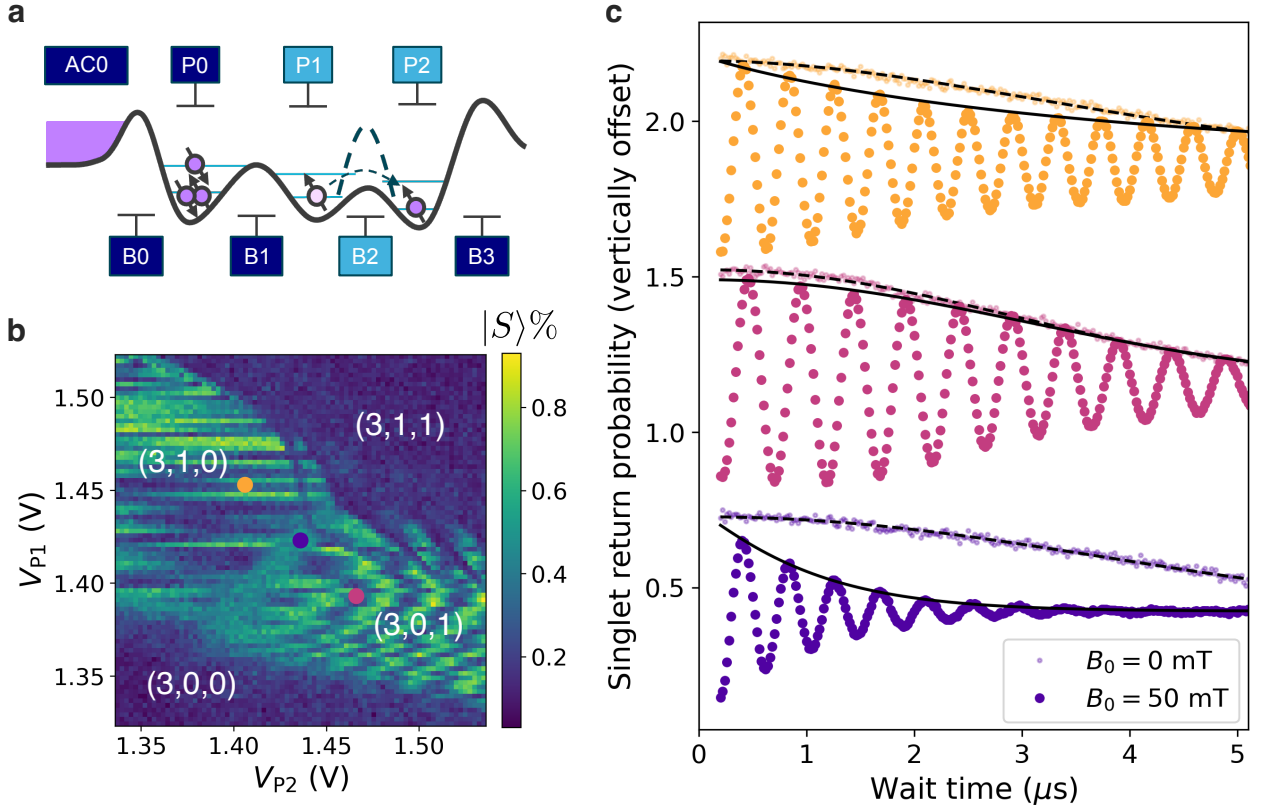


Figure 2. Shuttling and inhomogeneous dephasing. **a.** Cartoon representation of an electron being shuttled from QD1 to QD2. **b.** Singlet return probability ($|S\rangle\%$) during shuttling the detuning space surrounding the (3,1,0)-(3,0,1) charge transition. Three colored dots represent P1-P2 detunings corresponding to measurements shown in **c.** **c.** Inhomogeneous dephasing of the singlet return probability over time spent at three detunings: (3,1,0) (gold), (3,0,1) (pink) and at the charge transition (violet). Data at $B_0 \approx 0$ (50) mT are shown as small translucent (large opaque) circles, with decay envelope fits to Eq. 3 overlaid as dashed (solid) lines. Curves are vertically offset for clarity. Full fit parameter values and uncertainties are tabulated in Supplementary Table II.

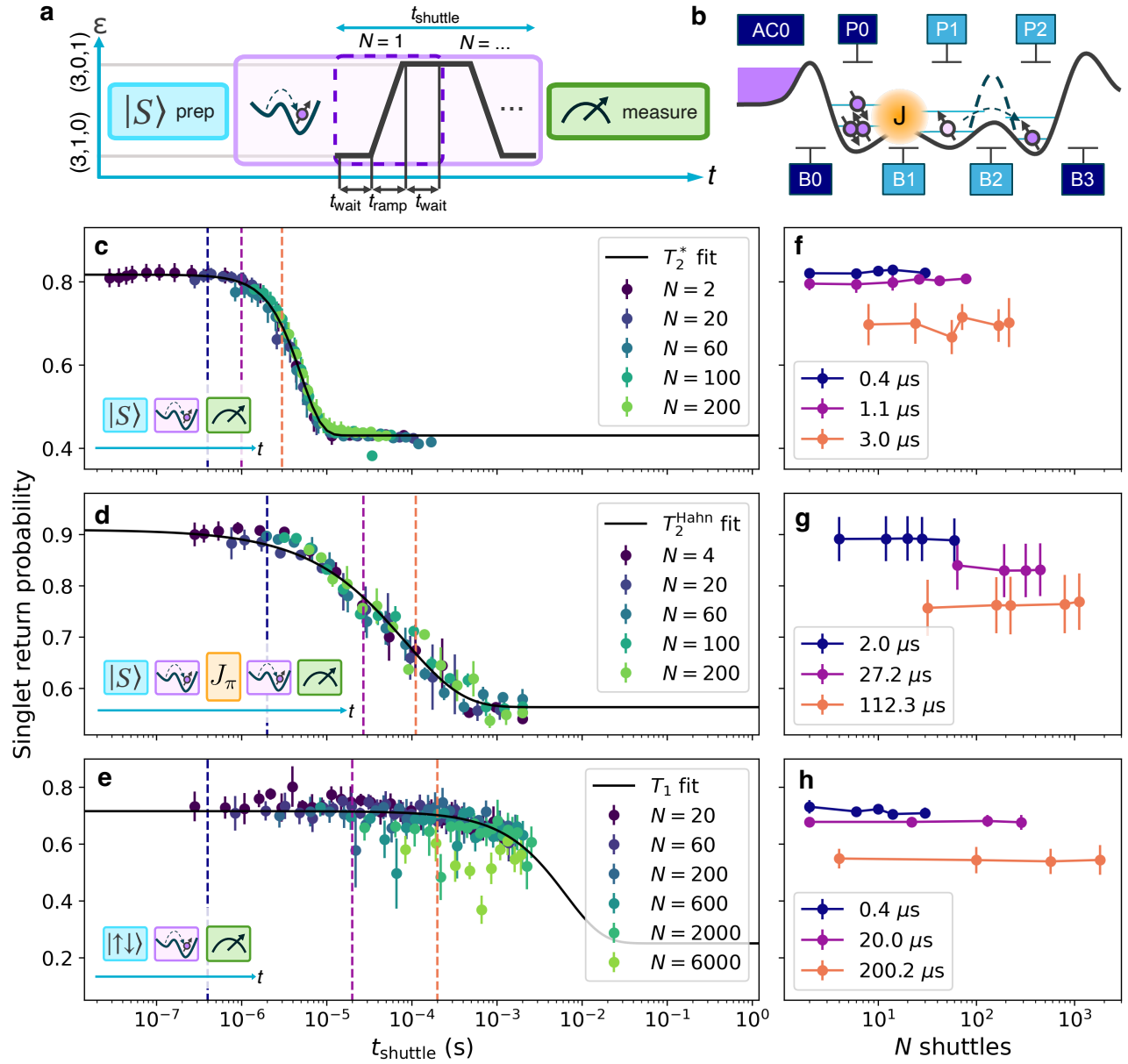


Figure 3. Repeated shuttling experiments. **a**. Pulse sequence diagram for repeated shuttles. A $|S\rangle$ state is prepared, undergoes shuttling between QD1 and QD2, and then its final spin state is measured. **b**. Cartoon representation of the exchange interaction between QD0 and QD1,2 used to carry out a π_z pulse for dynamical decoupling. **c**. Singlet return probability after N shuttles (different colored markers) are executed over a range of time. A fit of the form of Eq. 3 is overlaid (black curve). **d**. Singlet return probability for an experiment similar to **c**, but with the dynamical decoupling sequence shown in the inset applied. A fit of the form of Eq. 5 is overlaid (black curve). **e**. Singlet return probability for a $|\uparrow\downarrow\rangle$ state after N shuttles executed over time. An exponential decay fit of the form of Eq. 6 is overlaid (black curve). **f**, **g**, **h**. Repeated shuttles carried out at fixed t_{shuttle} corresponding to the colored vertical dashed lines in **c**, **d**, and **e**, respectively. $B_0 \approx 0$ mT for the $|S\rangle$ shuttles (**c**, **d**, **f**, **g**.) and $B_0 = 10$ mT for the $|\uparrow\downarrow\rangle$ shuttles (**e**, **h**). All error bars shown represent the standard deviation of the mean of the measurement.

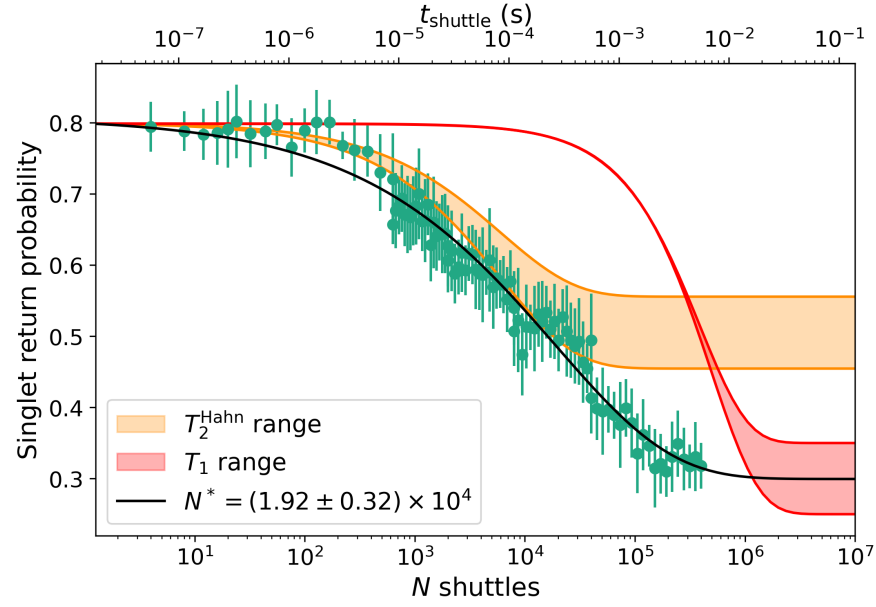
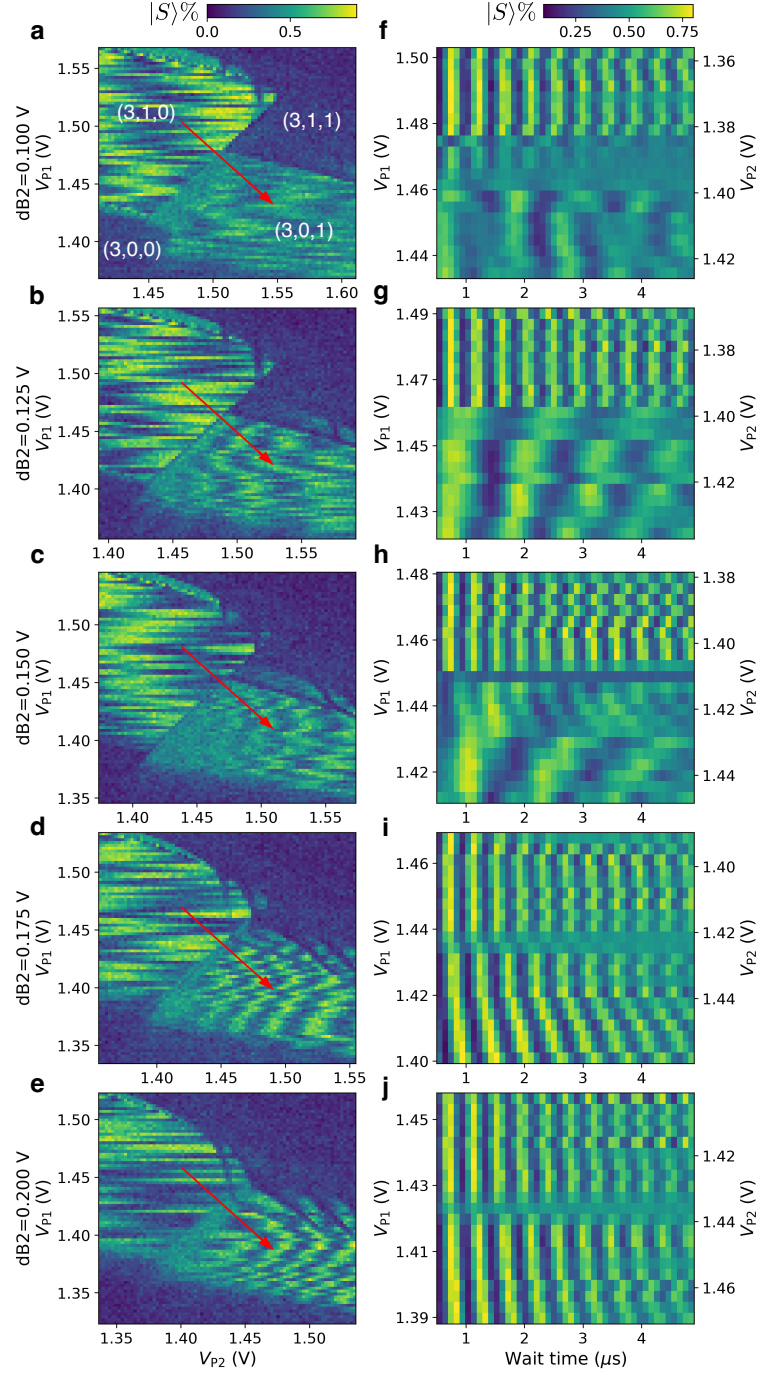
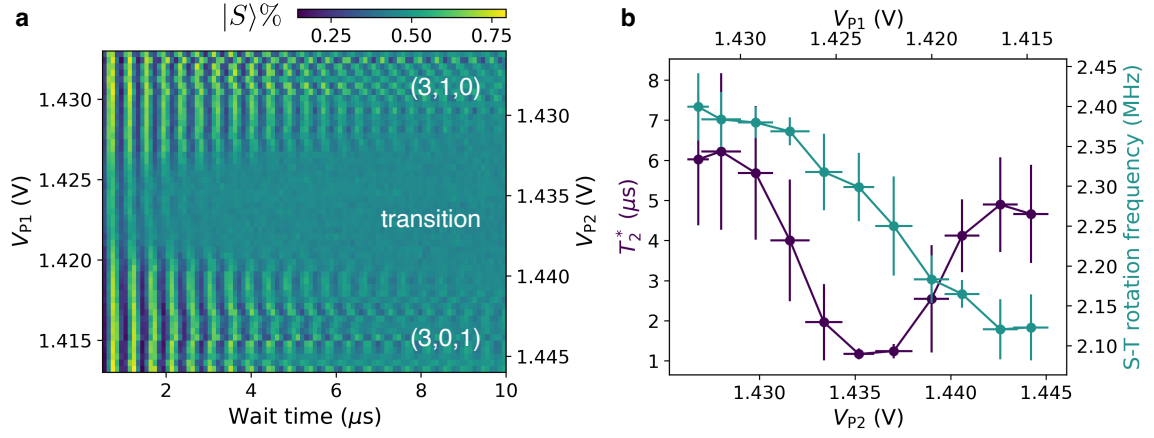


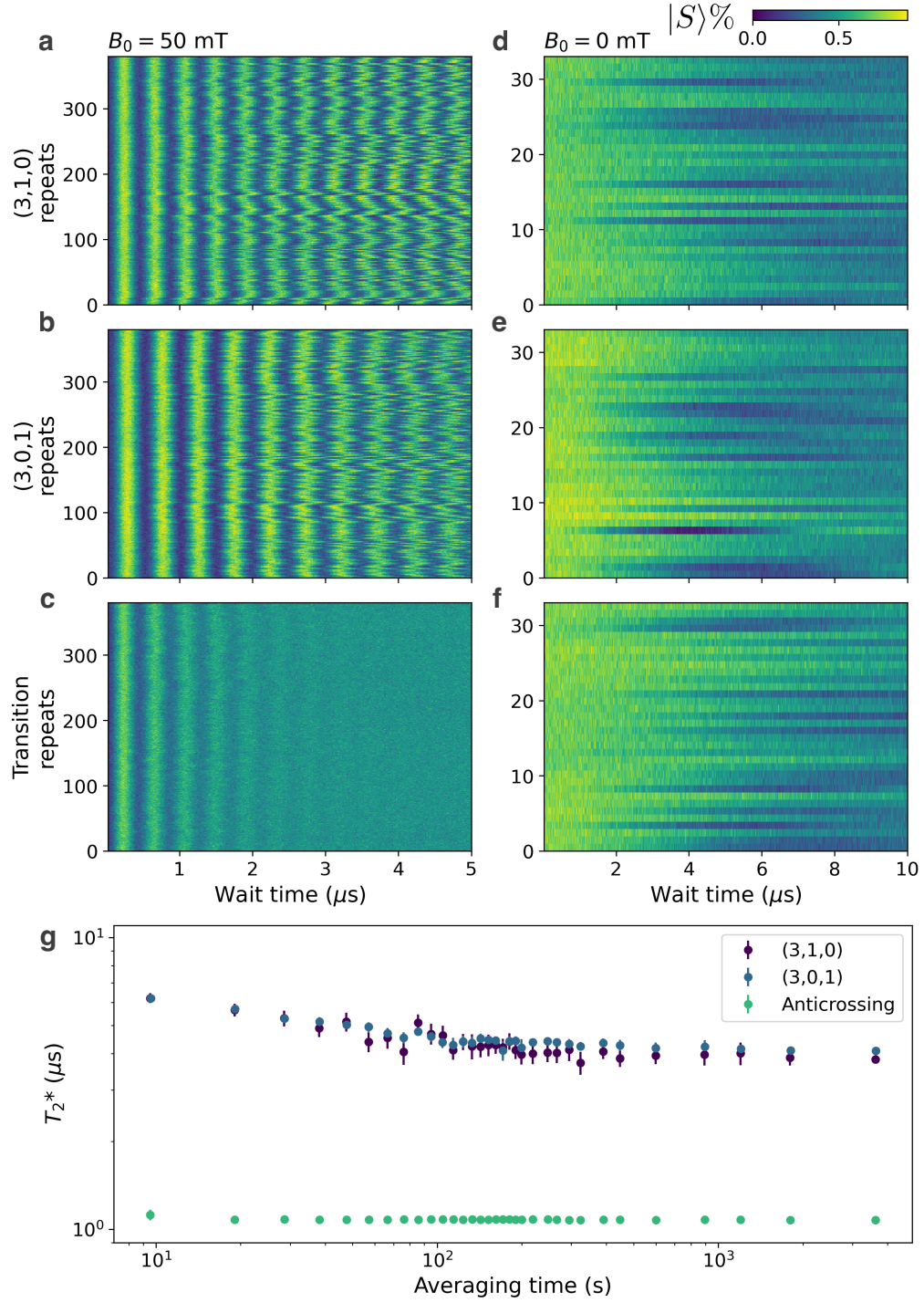
Figure 4. Shuttling error estimates at large N . Data is shown in teal markers where error bars represent standard deviations of the mean of multiple repeated measurements. A phenomenological fit of the form of Eq. 7 is overlaid (black curve). The range of T_2^{Hahn} (T_1) based on analysis in the main text regarding Fig. 3d. (Fig. 3e.) is shown in orange (red) shading, presented as a guide to the eye. The top horizontal axis (t_{shuttle}) is related to the bottom (N shuttles) by the expression $t_{\text{shuttle}} = N(2t_{\text{wait}} + t_{\text{ramp}}) = 14N$ ns. Here, $B_0 \approx 0$ mT.



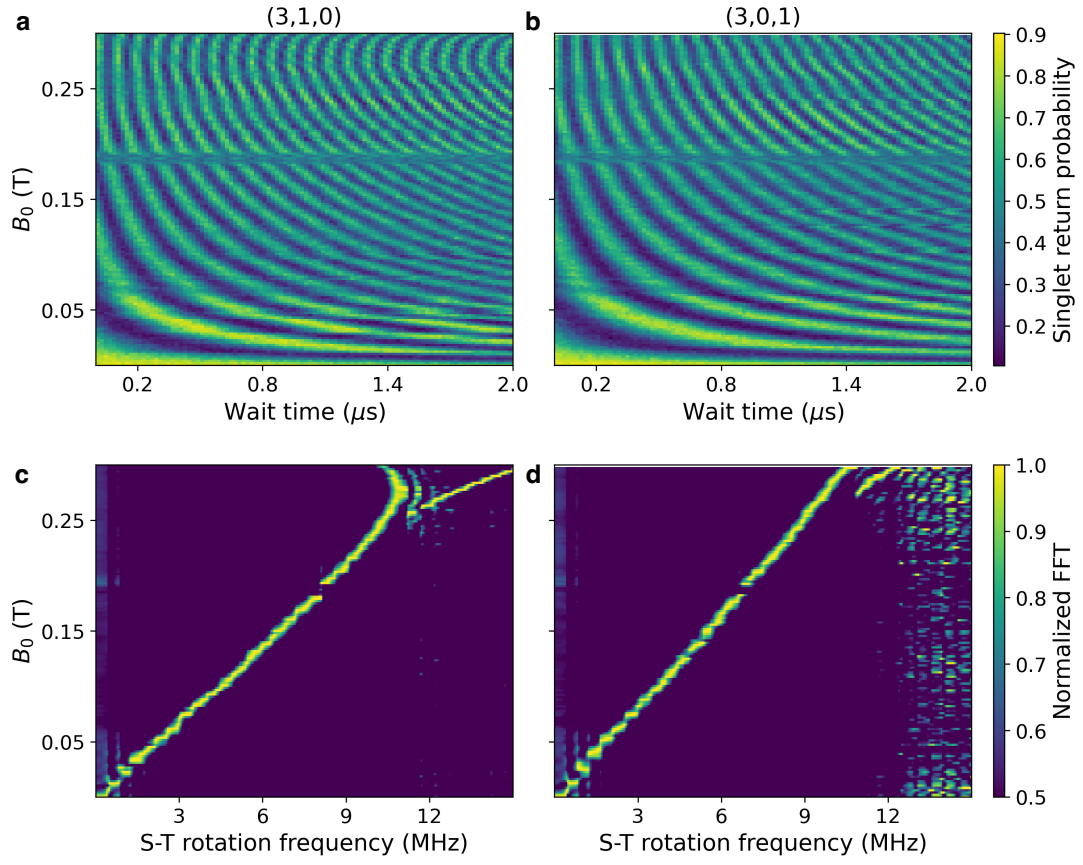
Supplementary Figure 1. Barrier-enhanced coherent spin transfer. **a.-e.** Singlet return probability raster scans of the charge space between (3,1,0) and (3,0,1) states for a range of barrier pulse voltages $dB2 = 0.1 - 0.2$ V used during the shuttle. The wait time in each panel is $6 \mu s$. **f.-j.** Singlet return over time as the detuning is ramped from (3,1,0) to (3,0,1) along the trajectory defined by red arrow in the corresponding raster plot shown in the panel directly to the left. $B_0 = 50$ mT and the detuning ramp time is 30 ns in all measurements shown.



Supplementary Figure 2. Shuttling from QD1 to QD2. **a.** Singlet return probability over time as the detuning is ramped from $(3,1,0)$ to $(3,0,1)$. **b.** Averaged fit parameters of T_2^* dephasing time (left y-axis) and S - T_0 rotation frequency (right y-axis) from a dephasing sine model (Eq. 4 with $\alpha = 2$) fit to the data in **a**.



Supplementary Figure 3. T_2^* repeated measurements spanning 1 hour. **a.-c.** Repeated time traces of singlet return probability for $(3,1,0)$, $(3,0,1)$ and the charge transition, respectively, at $B_0 = 50$ mT. **d.-f.** Repeated time traces of singlet return probability for $(3,1,0)$, $(3,0,1)$ and the charge transition, respectively, at $B_0 \approx 0$ mT. **g.** Gaussian T_2^* fits to each line trace over time in **a.-c.** averaged over an increasing number of line traces. The averaging time on the horizontal axis is derived from the lab time accumulated over the course of data acquisition, including dead time to read out and send information to the computer. T_2^* fits approach the ergodic limit after about 10 minutes of averaging.



Supplementary Figure 4. S - T_0 oscillations in an external magnetic field for (3,1,0) and (3,0,1) charge configurations. **a.-b.** Singlet return probability as B_0 is ramped. The qubit is held for a variable wait time in each of (3,1,0) and (3,0,1). **c.-d.** Corresponding normalized FFTs to the data shown in **a.,b.** showing S - T_0 qubit rotation frequency.